

Alginate-Mediated Mineralization for Ultrafine Hydroxyapatite Hybrid Nanoparticles

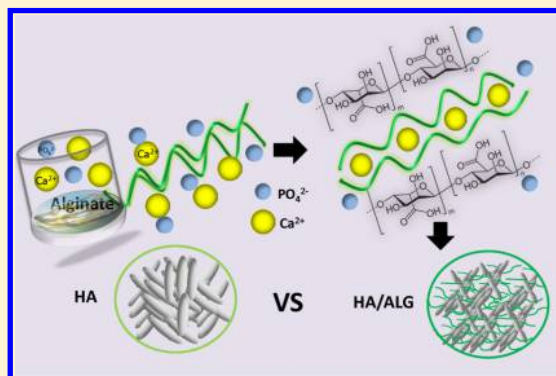
Xiaoxiang Ren,^{†,‡} Zhe Sun,[†] Xiaomin Ma,[†] Yanming Wang,[†] Xinxing Cui,[†] Zeng Yi,^{†,§} Xiaoyu Sun,[†] Bo Guo,^{*,§} and Xudong Li^{*,†,§}

[†]National Engineering Research Center for Biomaterials, Sichuan University, Chengdu 610064, P. R. China

[‡]Department of Biomedical Engineering, University of Groningen, Antonius Deusinglaan 1, 9713 Groningen, The Netherlands

[§]Department of Ophthalmology, West China Hospital, Sichuan University, Chengdu 610041, P. R. China

ABSTRACT: The good bioactivity of hydroxyapatite (HA) makes it become a popular biomaterial, and so, the synthesis of HA has attracted much attention. However, a simple method to prepare well-dispersive and ultrafine HA nanoparticles (NPs) still needs to be explored. Here, needle-like hybrid HA NPs were synthesized in the presence of alginate (ALG) and the mechanism of ALG regulation on forming HA/ALG hybrid NPs was investigated. The size and crystallinity of HA/ALG NPs could be controlled simply by varying the amount of ALG. With a higher concentration of ALG, the size of HA/ALG NPs reduced and their dispersity was further improved. The assembly with ca. 3–6 nm thick nanoneedles was discernible in HA/ALG NPs. The results collected by Ca^{2+} concentration, pH, and conductometric measurements further provided the supportive data for ALG inhibition of calcium phosphate compound formation and thus modulation of HA crystallization. In addition, the good biocompatibility of synthesized HA/ALG NPs was indicated from the results of CCK-8 assays and CLSM observations after cultured with L929 cells. The needle-like HA NPs are promising for varied biomedical purposes, and their potential application as drug carriers would be further studied.



1. INTRODUCTION

Hydroxyapatite (HA) ($\text{Ca}_{10}(\text{PO}_4)_6(\text{OH})_2$) is one of the most widely used bioceramics in the biomedical field because of its compositional similarity to natural bone.^{1–4} HA has attracted more and more attention because of its excellent biocompatibility, bioactivity, and osteoconductivity.⁵ Indeed, the excellent biological attributes of HA, such as nontoxicity and lack of inflammatory responses, have a close connection with the crystal size and morphology of synthetic HA.^{6–8} Especially, fine particles with a narrow size distribution are advantageous to biomedical applications.⁹ For example, hollow HA nanoparticles (NPs) were used as an advanced drug delivery carrier because of the unique pH sensitivity of HA.^{10–13} Furthermore, the nanosized HA crystal with a smaller size was reported to have the propitious effect on promotion of cell growth and inhibition of cell apoptosis.^{14,15} Therefore, it is quite important to find an effective and controlled method to obtain ultrasmall HA NPs with low crystallinity, which could be potentially used in the biomedical fields such as tissue engineering and drug controlled release. However, in the synthesis of HA, the immediate mixing of Ca^{2+} with PO_4^{2-} usually causes the uncontrolled rapid growth of calcium phosphates (CaP). This inevitable event makes it difficult to obtain well-dispersive nanosized HA precipitates except irregular agglomerates.

Among varied synthetic methods of HA, such as chemical precipitation,¹⁶ sol–gel technique¹⁷ and hydrothermal treat-

ment,¹⁸ the use of organic matters especially natural polysaccharides as growth modifiers is demonstrated to be an efficient strategy to control preparing HA.^{19–21} This organic-mediated synthesis strategy usually gives rise to organic–inorganic hybrid nanomaterials, which are of great interest in the field of biotechnology for their unique properties.^{22–24} Alginate (ALG), a natural polysaccharide extracted from brown sea algae, belongs to a family of unbranched binary copolymers with a structure of 1–4 glycosidically linked β -D-mannuronic acid (M unit) and C-5 epimer α -L-guluronic acid (G unit)^{30–36} and is widely used in food, surgical, pharmaceutical, and cosmetic fields.^{25–29} Owing to its good biocompatibility and unique cross-linking with Ca^{2+} , ALG becomes a good selection for organic modulation of HA. ALG bound with monovalent ions is generally water-soluble, while its “egg-box” structural hydrogels with bivalent cations such as Ca^{2+} are partially soluble in water.^{37–39} In fact, calcium cross-linked ALG hydrogels have been used in many biomedical applications, including tissue engineering and drug delivery.^{40,41} Meanwhile, ALG was also used to modulate the synthetic process of HA. Wang⁴² et al. synthesized HA/ALG nanocomposites, in which HA aggregates are embedded in the ALG matrix by in situ hybridization. The

Received: January 16, 2018

Revised: April 18, 2018

Published: May 17, 2018

crystallinity of HA was found to decrease with a higher ALG addition, and the crystallites tended to elongate along *c*-axis. Lin⁴³ et al. prepared porous ALG/HA scaffolds through phase separation. Coleman⁴⁴ et al. also studied the inhibition effect of ALG on HA growth, but no obvious effect on crystal growth was found. Most of these studies focused merely on the cross-linking role of Ca²⁺ with ALG and were lack of physicochemical homogeneity. HA materials prepared by these methods were generally larger than 100 nm with the presence of obvious agglomeration, although ALG was introduced in HA synthesis systems. Few reports were associated with obtaining HA with the size smaller than 10 nm. Besides, the role of ALG in the growth of HA is still need to be explored.

Inspired by these studies, we have previously synthesized rodlike HA nanocrystals via the hydrothermal method,⁴⁵ in which the intervened role of ALG for hydrothermally prepared HA was confirmed. However, such HA NPs have poor dispersive stability in water and low specific surface areas, limiting their potential applications. In addition, ALG would decompose under hydrothermal conditions, and thus, the biological effect of ALG would be absent in the hydrothermally synthesized HA. Herein, novel ultrasmall HA/ALG nanoneedles with some inherent biological properties of ALG were prepared in ambient environment, and the modulation effect of ALG on HA synthesis at room temperature (RT) was further investigated with the aid of calcium ion electrode and conductometric measurements. These HA/ALG nanoneedles were about 40–80 nm in length and 8–12 nm in width, which were assembled actually by much smaller needle-like NPs of 3–6 nm in width. In contrast, such ultrafine HA NPs were seldom reported in published studies. This successful ultrafine HA synthesis confirmed that ALG plays an important modulation effect, and the unique biomedical performance of these HA/ALG nanohybrids would be further investigated.

2. EXPERIMENTAL SECTION

2.1. Preparation of HA/ALG NPs. All chemical reagents were of analytical grade and used as received without any further purification. To obtain hybrid HA/ALG NPs, 0.16 g of ALG powder was dissolved in 40.0 mL of deionized water, and the mixture was stirred overnight to form a homogeneous ALG solution. Then, 2.0 mL of 1.0 M CaCl₂ solution was added in drops into the ALG solution. After that, a vortex (IKA, Vortex, Genius 3) was used to stir the mixture solution to obtain a homogeneous blend. Subsequently, 2.0 mL of 0.6 M NaH₂PO₄ aqueous solution was further added slowly with continuous stirring. The pH of the reaction blend was adjusted to approximately 12.0 by addition of 2.0 M NaOH. In this procedure, the pH value and the conductivity value were monitored. This mixture was left at RT for 1 week. At the same time, the change of conductivity was observed in the period of initial 50 h. HA/ALG NPs were finally collected by centrifugation and rinsed with deionized water for several times. The collected precipitates were freeze-dried for further analyses. In the present study, four different types of HA NPs were prepared with ALG concentrations varying from 0, 0.2, 0.4 to 0.8 wt %, and the samples were thereafter designated as HA-control, HA/ALG-0.2%, HA/ALG-0.4%, and HA/ALG-0.8%, respectively, where HA-control represents the control sample without using ALG.

2.2. Characterization. Transmission electron microscopy (TEM) and high resolution TEM (HRTEM) images were taken using a Tecnai G2 F20 S-TWIN transmission electron microscope to examine the microstructural morphology of different samples and also to verify their crystallographic structure.

X-ray diffraction (XRD) analyses were conducted on a DX-1000 X-ray diffractometer with CuK α radiation ($\lambda = 1.5406 \text{ \AA}$) to confirm specific calcium phosphate phases. The XRD patterns were recorded at the working voltage and current of 40 kV and 25 mA.

Fourier transform infrared spectroscopy (FT-IR) was measured with KBr pellet methods on a PerkinElmer Spectrum One B system. The spectrum was collected in the wavenumber range of 4000–400 cm⁻¹ for the assignment of the molecular species of the samples.

Thermogravimetric analysis (TGA) was performed on a Netzsch thermal analyzer STA 449C, and the samples were examined under a nitrogen atmosphere at a constant rate of 15 °C min⁻¹ in the scanning range of RT to 1200 °C with an empty aluminum pan as a control.

The specific surface areas of the samples were measured on a micromeritics Gemini instrument by using Brunauer–Emmett–Teller (BET) nitrogen absorption.

The variation of zeta potential of the NPs in phosphate buffer solution (0.5 mg/mL, ionic strength = 0.01 M) was determined by Malvern Zetasizer Nano biological examination.

2.3. Role of ALG in Modulating CaP Precipitation. To investigate the interactions between Ca²⁺, phosphate, and NaOH, a series of experiments were performed with different Ca²⁺ concentrations. In a typical experiment, 40 mL of 1000 mg/L CaCl₂ solution was prepared, and then, Na₂HPO₄ solution was added to make the final Ca/P ratio around 1.67. After that, 2.0 M NaOH was added drop by drop into the above solution. At the same time, the Ca²⁺ concentration and the pH value were recorded using the calcium ion electrode. Similarly, another two experiments were also performed with the concentration of CaCl₂ set to 2000 and 3000 mg/L.

To study the influence of ALG on CaP precipitation for a long time, 0.8 wt % ALG solution with 1.0 mL of 1.0 M CaCl₂ and 1.0 mL of 0.6 M Na₂HPO₄ was prepared. Then, 2.0 M NaOH was added, and the change of conductivity of the reactions was monitored for up to 250 h. Similarly, the amount of either CaCl₂ or Na₂HPO₄ was reduced to 0.5 mL to perform the same experiment. In addition, a control group which only contains ALG without CaCl₂ and Na₂HPO₄ was also set, whereas a blank group with 1.0 mL CaCl₂ and 1.0 mL Na₂HPO₄ without ALG was also set.

To further confirm the interactions between ALG and HA, the conductivity and pH experiments of ALG at various concentrations from 0 to 0.8 wt % in the presence of 2 mL of 1 M CaCl₂ and 2 mL of 0.6 M Na₂HPO₄ were performed. NaOH (2 M) was introduced drop by drop to adjust the pH value of the reaction to 12. The conductivity and pH values for the systems were measured during this period with a Mettler Toledo conductometer (SevenMulti, Mettler Toledo, Switzerland).

2.4. Cell Culturing. L929 cells were grown in Dulbecco's modified Eagle medium (DMEM; Gibco) supplemented with 10% FBS and 1% penicillin/streptomycin and cultured in an incubator with 5% CO₂ atmosphere at 37 °C. The cytotoxicity of HA NPs was tested by the CCK-8 assay. L929 cells were separately seeded into 96-well plates at a cell density of 5×10^3 cells per well with 100 μ L of DMEM medium. After 24 h incubation, the culture medium was removed and replaced with 100 μ L of a medium-containing HA-control, HA/ALG-0.2%, and HA/ALG-0.4% at the concentration of 200 μ g/mL, and the cells were further incubated for 1, 3, and 5 days. Then, the cells were washed three times with PBS and replaced with fresh culture medium. CCK-8 kit (10 μ L) was then added into each well. After 4 h of incubation, the absorbance of the product was measured at 492 nm using a microplate reader (Thermo Fisher Scientific, Varioskan Flash).

To perform the fluorescent staining assay, confocal laser scanning microscopy (CLSM, Leica-TCS-SP5, Germany) was employed. For this purpose, L929 cells were seeded in 24-well plate (2×10^4 cells per well) and then co-cultured with 200 μ g/mL of the HA-control, HA/ALG-0.2%, HA/ALG-0.4% NPs, respectively. Cells cultured without HA-NPs were used as control, and all assays were performed in triplicate. Before observation, the original culture medium was removed and the attached cells were stained by fluorescein diacetate (FDA, Sigma, USA) for live cells (green) and propidium iodide (PI, Sigma, USA) for dead cells (red).

3. RESULTS AND DISCUSSION

3.1. HA/ALG NPs Structural Characteristics. XRD patterns of the synthesized HA samples are shown in Figure

1 together with the standard diffraction data of HA (JCPDS09-0432). Obviously, HA-control, HA-0.2%, HA-0.4%, and HA-

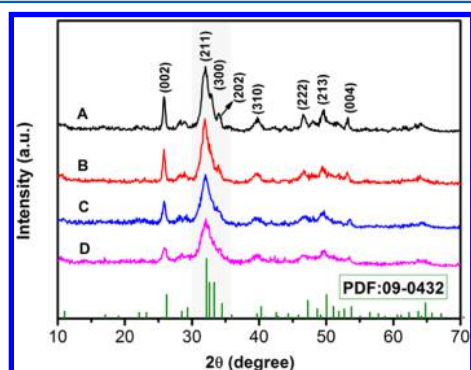


Figure 1. XRD patterns of the samples synthesized from the CaP solutions containing ALG concentration varying from (A) 0.0% (HA-control), (B) 0.2% (HA/ALG-0.2%), (C) 0.4% (HA/ALG-0.4%), and (D) 0.8% (HA/ALG-0.8%).

0.8% samples have similar diffraction peaks, which correspond well to the standard data of crystalline HA with no evidence of secondary crystal phases. The relatively strong peaks of HA-control at $2\theta = 26.02, 31.96, 33.10, 34.24, 39.88, 46.90, 49.60,$ and 53.38° correspond to (002), (211), (300), (202), (310), (222), (213), and (004) planes of HA, respectively. Diffraction peaks of (211), (300), and (202) are discernible as three individual peaks in HA-control, whereas a broad reflection with the maximum at $2\theta = 31.9^\circ$ appears in the HA/ALG samples. This comparison suggests that the crystallinity of synthesized HA/ALG NPs is much lower than that of HA-control. In fact, the diffraction intensity of both (002) plane and (211) plane shows an obvious decrease from the top (A) sample (HA-control) down to the (D) sample (HA-0.8%) (Figure 1), and these peaks also tend to be broadened, indicative of the reduction of the crystallinity of the synthesized samples along with a higher addition of ALG. The crystallinity calculated from XRD data is given in Table 1. Without using ALG, the obtained

Table 1. Crystal Lattice Constants and Crystallinity of the Synthesized Samples Calculated from XRD Data

sample	<i>a</i>	<i>b</i>	<i>c</i>	crystallinity (%)
HA-control	9.4375	9.4375	6.8668	54.98
HA/ALG-0.2%	9.4274	9.4274	6.8983	45.39
HA/ALG-0.4%	9.3387	9.3387	6.8763	36.41
HA/ALG-0.8%	9.3337	9.3337	6.8760	30.24

HA-control sample holds the highest crystallinity of 54.98%. In contrast, the crystallinity of three HA/ALG samples is relatively low, 45.39% for HA/ALG-0.2, 36.41% for HA/ALG-0.4%, and 30.24% for HA/ALG-0.8%, following a ALG concentration-dependent decrease trend. In addition, slight alterations in the crystal lattice constants exist between HA-control sample and three HA/ALG samples (Table 1), further validating the incorporation of ALG into HA.⁴⁵ Relative to those of HA-control, a decrease in $a = b$ values is more significant than in c values among all the HA/ALG samples.

To ascertain the chemical species of the synthesized HA, the FT-IR spectra of HA-control, HA/ALG-0.2%, HA/ALG-0.4%, HA/ALG-0.8%, and ALG are illustrated in Figure 2. In HA-control sample, the adsorptions at 567, 603, and 1035 cm^{-1} are

due to PO_4^{3-} stretching vibrations of HA, and the 3575 cm^{-1} adsorption is from the stretching vibration of the hydroxyl group of HA. Along with those typical bands of HA, some changes also occurred in HA/ALG samples. With increasing ALG, the adsorption at around 1619 cm^{-1} obviously tends to be stronger in HA/ALG-0.2%, HA/ALG-0.4%, and HA/ALG-0.8% samples (Figure 2a), indicative of partial incorporation of ALG into HA NPs. This ascertainment is supported by the detection of the adsorptions at 1619 and 1415 cm^{-1} for Ca^{2+} -bound ALG, while the stretching vibrations of C–O bonds from the carboxylate group in ALG give sharp peaks at 1614 and 1404 cm^{-1} (Figure 2b).⁴⁵

TGA thermograms of HA-control, HA/ALG-0.2%, HA/ALG-0.4%, HA/ALG-0.8%, and pure ALG samples are given in Figure 3, indicating a multistage weight loss for all the samples. As shown in Table 2, the weight loss in the range of RT–180 $^\circ\text{C}$ is related to the release of adsorbed water which is very similar in all the samples. The loss in 180–300 $^\circ\text{C}$ is caused by dehydrated bound water and initially decomposed organic species. Thus, pure ALG gave the highest weight loss and in HA/ALG samples, this value tends to be lower along with a less ALG dosage. The weight loss in 300–650 $^\circ\text{C}$ is due to a further evaporation of the organic components. Above 650 $^\circ\text{C}$, the weight loss in HA samples is also arisen from the decomposition of carbonates incorporated in HA. At 1200 $^\circ\text{C}$, the residual weight percentage is 87.03% for HA-control, 17.82% for ALG, 79.52% for HA/ALG-0.2%, 69.92% for HA/ALG-0.4%, and 64.42% for HA/ALG-0.8%. Correspondingly, the approximate ALG residue is 1.93% for HA/ALG-0.2%, 4.40% for HA/ALG-0.4%, and 5.82% for HA/ALG-0.8%.

Figure 4a gives the N_2 adsorption/desorption isotherms of synthesized HA-control, HA/ALG-0.2%, HA/ALG-0.4%, and HA/ALG-0.8% samples. As shown in Table 3, the specific surface areas and pore volumes of the HA-control sample are 100.83 m^2/g and 0.593 cm^3/g , which is much higher than HA NPs synthesized by hydrothermal treatment.⁴⁵ However, compared with HA-control, specific surface areas are notably increased after the introduction of ALG for preparing HA/ALG-0.2%, HA/ALG-0.4%, and HA/ALG-0.8%. All these values are over 120 m^2/g . In fact, all the samples present similar type VI isotherms and typical H1 hysteresis loops, the typical attributes of mesoporous materials. The high surface area, mesoporous structure, and nanoscale size are known to be beneficial for the potential application as drug delivery. Moreover, zeta potential is an important parameter to evaluate the stability of NPs in solutions. The measured zeta potential values of HA-control, HA/ALG-0.2%, HA/ALG-0.4%, and HA/ALG-0.8% are shown in Figure 4b. Obviously, the zeta potential of the NPs decreased with a higher ALG concentration. In the HA-control sample, the zeta potential of the NPs is slightly positive. Yet, when it comes to the HA/ALG-0.8% sample, the zeta potential is already -29.5 mV. The zeta potential variation of the NPs is attributed to the COO^- and OH^- of ALG. Accordingly, the incorporation of ALG into HA is responsible for the negative charges on the surfaces of HA/ALG NPs, which ensure their good dispersibility and stability in water. As shown in the inset photo of Figure 4b, HA/ALG-0.4% and HA/ALG-0.8% samples are still well-dispersive in water after standing still for 1 week. In contrast, obvious sedimentation is observed in HA-control.

TEM images of different HA NPs with a different content of ALG are shown in Figure 5. Figure 5a–d reveals that the formed HA nanocrystals are quite small and present in the

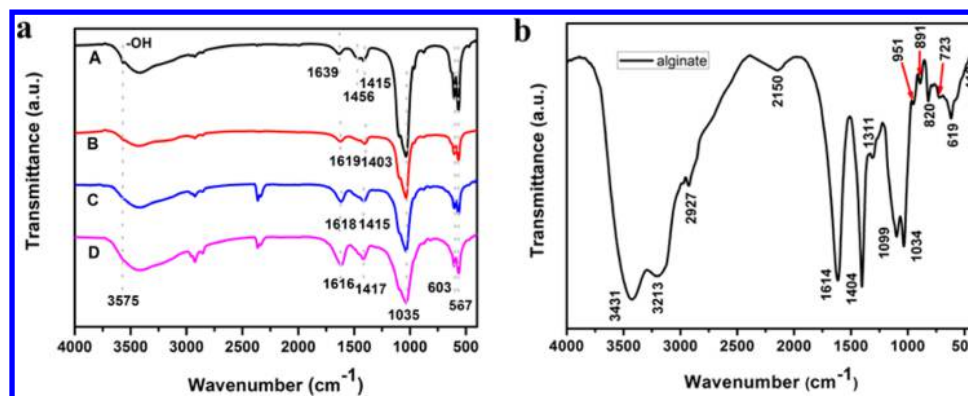


Figure 2. (a) FT-IR spectra of the samples synthesized from CaP solutions containing a varying ALG concentration: (A) HA-control; (B) HA/ALG-0.2%; (C) HA/ALG-0.4%; and (D) HA/ALG-0.8%. (b) FT-IR spectrum of pure ALG.

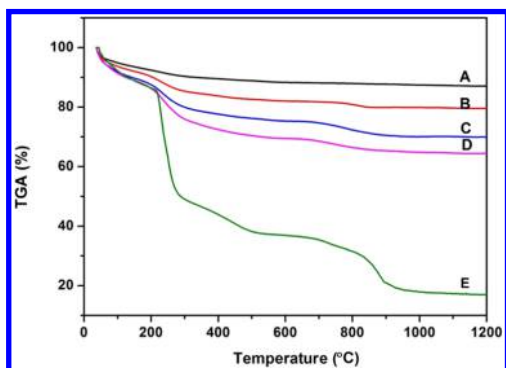


Figure 3. TGA thermograms of synthesized samples from CaP solutions containing a varying ALG concentrations: (A) HA-control; (B) HA/ALG-0.2%; (C) HA/ALG-0.4%; (D) HA/ALG-0.8%; and (E) pure ALG.

Table 2. Weight Loss of the Synthesized Samples in Different Multistage Obtained from TGA Data

temperature (°C)	0–180	180–300	300–650	650–1200
HA-control (%)	7.19	9.69	11.82	12.97
HA/ALG-0.2% (%)	8.97	14.69	18.08	20.48
HA/ALG-0.4% (%)	11.5	20.06	24.82	30.08
HA/ALG-0.8% (%)	12.46	24.04	30.77	35.58
pure ALG (%)	12.2	51.2	62.87	82.18

Table 3. Specific Surface Areas and Pore Volumes of Different Samples

sample	V_p (cm ³ /g)	S_{BET} (m ² /g)
HA-control	0.593	100.83
HA/ALG-0.2%	0.586	122.53
HA/ALG-0.4%	0.476	126.17
HA/ALG-0.8%	0.326	125.15

rodlike shape or needle-like shape. Especially, HA/ALG NPs are much finer with containing a higher ALG concentration. The selected area electron diffraction (the inset in Figure 5a) of synthesized HA-control reveals that these nanocrystals are weakly crystallized. As shown in the magnified images in Figure 5a1–d1, these HA NPs are actually assembled by extremely tiny needle-like particles. The size of these tiny particles is obviously different among samples, as typically circled and further schematically illustrated in Figure 5. Comparatively, the HA-control particles are much bigger than those HA/ALG samples, especially that containing a higher ALG content. To quantify the size of these ultrasmall needle-like particles, 30 particles in Figure 5a1–d1 were randomly selected to measure their width, and the average size of these NPs is shown in Figure 5e. It is evident that significant differences exist between HA-control and HA/ALG samples, especially with 0.4 and 0.8% addition of ALG. The width of HA-control is about 7 nm, and the value gradually decreased with increasing ALG concentration. In HA/ALG-0.8%, the width of these particles is only around 3 nm. Because the boundaries of these ultrasmall

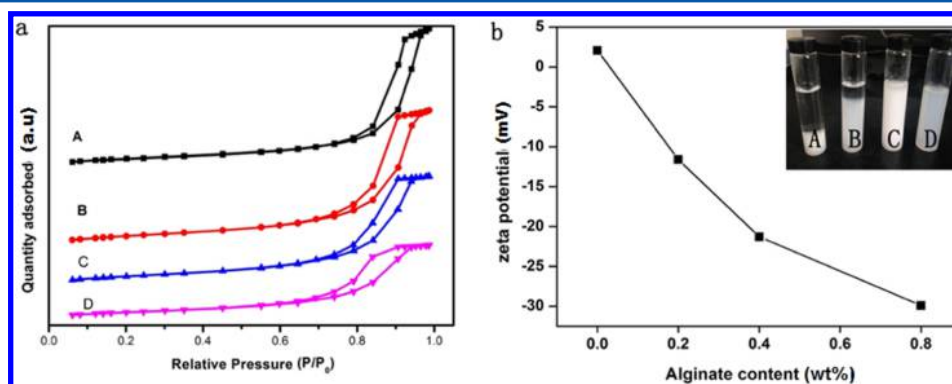


Figure 4. (a) N₂ adsorption/desorption isotherms and (b) zeta potential of synthesized samples from CaP solutions containing a varying ALG concentration: (A) HA-control; (B) HA/ALG-0.2%; (C) HA/ALG-0.4%; and (D) HA/ALG-0.8%. The photo in the inset shows respective colloidal stability of synthesized samples dispersed in water for 1 week.

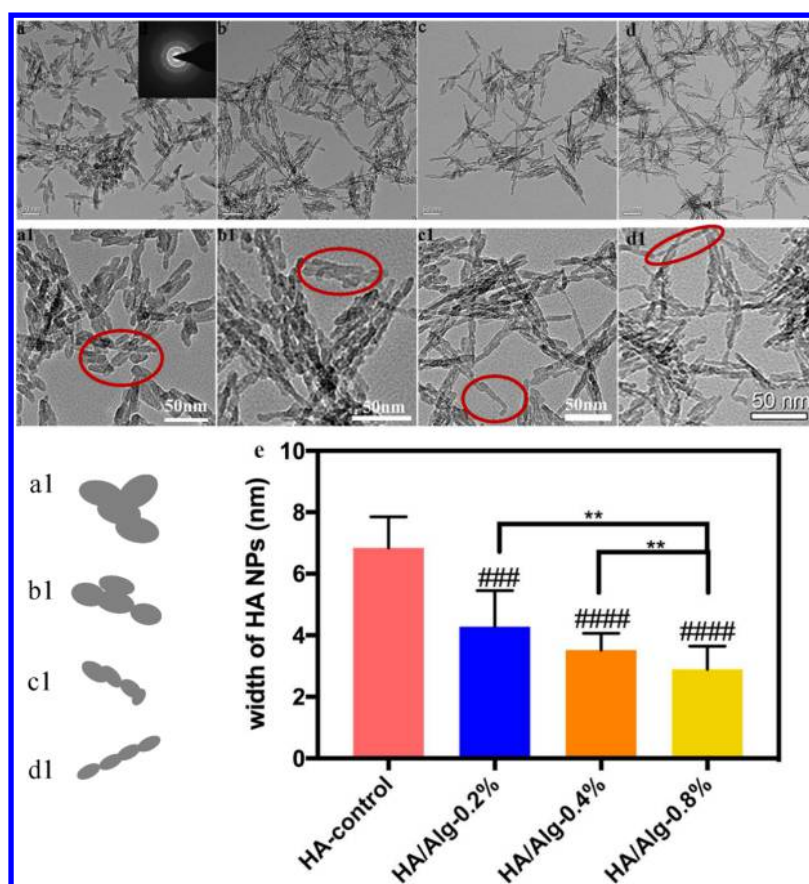


Figure 5. TEM images of the synthesized samples: (a,a1) HA-control, (b,b1) HA/ALG-0.2%, (c,c1) HA/ALG-0.4%, (d,d1) HA/ALG-0.8%, and (e) width of HA NPs (#indicates a significant different with HA-control group, *indicates a significant difference between groups, ** $p < 0.01$, ### $p < 0.005$, #### $p < 0.001$).

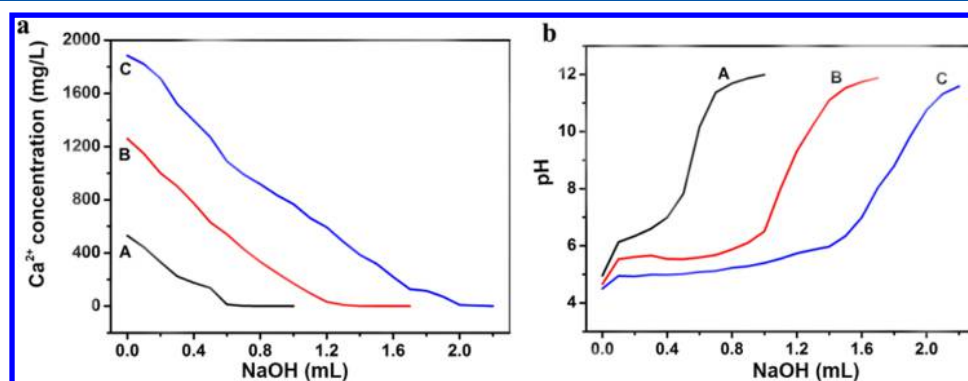


Figure 6. Change of (a) Ca^{2+} concentration and (b) pH value with NaOH addition in solutions containing (A) 1000, (B) 2000, and (C) 3000 mg/L Ca^{2+} concentration in the presence of equivalent PO_4^{3-} .

nanosized needles in HA/ALG-0.4% and -0.8% samples are hard to recognize, no definite value could be given to the length values of these ultrasmall particles. However, judged from these images, the introduction of ALG is shown to decrease the length of HA particles. The formation of the HA/ALG NPs assembled by ultrasmall nanosized needles probably explains why these NPs have very high specific surface areas. HA NPs with this advantageous feature are especially useful for achieving a considerably high drug-loading efficiency.

3.2. Possible Modulation Effects of ALG. All these results above together with our previous studies^{31,45} have shown the important intervention role of ALG in the synthetic reaction of HA. To further confirm it, we have monitored the

change of Ca^{2+} concentration, pH value, and conductivity of the synthetic reactions for HA/ALG NPs. The measurements were carried out in a mixture of ALG, CaCl_2 , and Na_2HPO_4 solutions with addition of NaOH at RT.

Firstly, the reaction between Ca^{2+} , PO_4^{3-} , and NaOH without ALG was investigated. Figure 6a illustrates the change of Ca^{2+} concentration with addition of NaOH, measured by using the calcium ion electrode. The Ca^{2+} concentration nearly linearly dropped to zero with the addition of OH^- no matter how much Ca^{2+} existed in the original solution. It confirmed that in the previous experiments the addition of around 1.6 mL NaOH would nearly consume all the Ca^{2+} and there would be no Ca^{2+} in the solution. The curves in Figure 6b showed a

similar trend that the pH value increased slowly at the first stage and then a sharp increase occurred. With a higher concentration of Ca^{2+} , it would consume more OH^- and the curve slope was smaller at the first period. This confirms that in the first part OH^- mainly reacted with Ca^{2+} to form the CaP compound. After Ca^{2+} was consumed entirely, the addition of NaOH leads to the sharp increase of pH.

Figure 7 shows the variation of conductivity of different reaction mixtures over time. From the results of Figure 6a, the

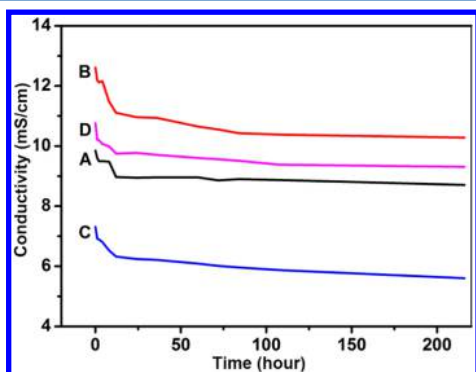


Figure 7. Time lapse curves of the conductivity in 0.8 wt % ALG-containing CaP solution groups: (A) 0.5 mL of 1.0 M CaCl_2 and 0.5 mL of 0.6 M Na_2HPO_4 , (B) 1.0 mL of 1.0 M CaCl_2 and 1 mL of 0.6 M Na_2HPO_4 , (C) blank group of (B) solution without using ALG, and (D) control group of ALG solution without CaP.

Ca^{2+} was absent in the solution after addition of 2 M NaOH. Thus, the conductivity was supposed to keep a stable value after a decrease in the first few minutes. However, as time went by, the conductivity of solution still decreased (Figure 7), especially in the initial few hours. This is because that at the first stage, Ca^{2+} reacts with PO_4^{3-} and OH^- to form insoluble calcium phosphate or $\text{Ca}(\text{OH})_2$. During this period, the calcium phosphate compound gradually accumulated, and both anions and cations in the solution were consumed. However, these inorganic compounds would slowly dissolve and react with additional ions from solution to transform to a more stable calcium phosphate precipitate such as HA. This transformation led to the continuous decrease of conductivity. Though ALG had an inhibition role in the formation of the Ca/P compound, a decrease of conductivity was also observed in the groups in the presence of ALG. On one hand, the consumption of Ca^{2+} ions may partly arise from the free Ca^{2+} in solution to react with PO_4^{3-} and OH^- . On the other hand, because the ALG

could capture the Ca^{2+} first, the so-called “egg-box” model may release some Ca^{2+} with time prolonged.

To study the interactions specifically, Figure 8 shows the variations of both pH and conductivity during NaOH addition to the CaP solutions of CaCl_2 and Na_2HPO_4 in the presence of different ALG concentrations. The trend in Figure 8a was similar to that revealed in Figure 6b. Initially, NaOH addition provided OH^- to form CaP, and after that, more OH^- then led to a huge increase of pH. Compared with the groups contained ALG, the pH value of the control group (without ALG) was lower at the beginning, indicating more OH^- was consumed. This corresponded to forming a large amount of white calcium phosphate precipitates the moment NaOH was added without using ALG. In contrast, no obvious precipitation was observed in the groups with ALG. In no ALG group, the Ca^{2+} would react only with PO_4^{3-} and OH^- , but in ALG groups, the Ca^{2+} would react with ALG, PO_4^{3-} , and OH^- . When ALG introduced, it competed with PO_4^{3-} and OH^- . ALG would inhibit the formation of calcium phosphate compound by reacting with Ca^{2+} to form an “egg-box” structure.^{46,47} However, after 0.6 mL of NaOH added, a sharp increase appeared in the group without ALG, which means less consumption of OH^- . At this time, the Ca^{2+} was almost consumed entirely and the CaP formation nearly ended. Thus, the addition of NaOH led to a sharp pH elevation. To the contrary, the pH value of ALG groups showed a slow but steady elevation before 1 mL NaOH addition. In this progress, ALG actually behaved to inhibit the reaction of the CaP compound, thus retarding the formation of CaP. Meanwhile, the consumption of OH^- also slowed down compared with that occurred in the blank group (without ALG).

The changes of conductivity in Figure 8b indicated the variations of anions and cations in the mixing solutions. As mentioned above, NaOH offers OH^- for calcium phosphate formation at the first stage. Thus, the ions in solution were consumed in this period, and the conductivity showed a decrease trend in all groups. After the Ca^{2+} ions were reacted completely, the further addition of NaOH would contribute to the increase of conductivity caused by the introduction of OH^- and Na^+ . However, the curves were still quite different among three groups, but the trend was in accordance with the pH changes given in Figure 8a. The conductivity of the control group without ALG dropped down sharply before 0.6 mL of NaOH was added, indicating that CaP formation already finished at this point. In contrast, ALG showed an obvious intervention role again, and in the CaP/ALG groups, the

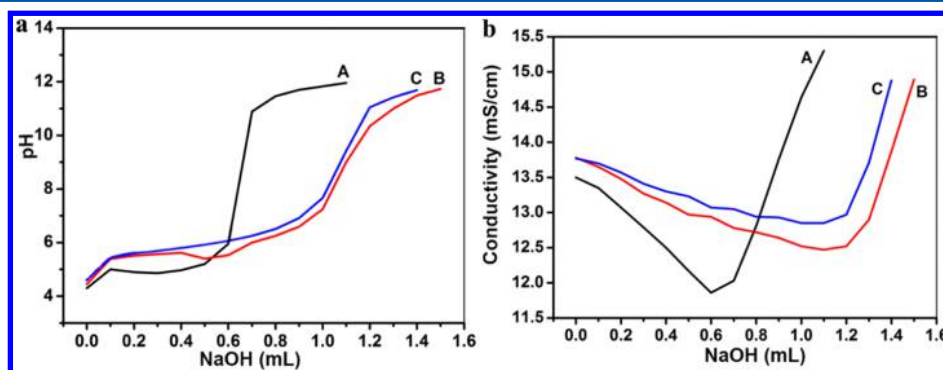


Figure 8. Change of (a) pH value and (b) conductivity with NaOH addition in CaP solutions of 2.0 mL of 1.0 M CaCl_2 and 2.0 mL of 0.6 M Na_2HPO_4 containing different ALG concentrations from (A) 0.0, (B) 0.4, and (C) 0.8 wt %.

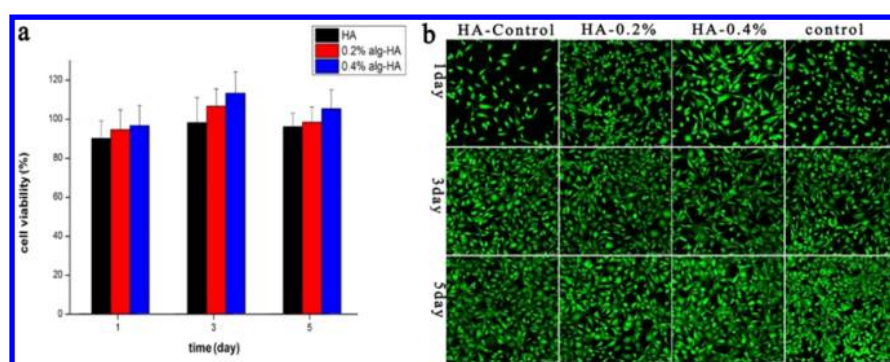


Figure 9. (a) In vitro viability (by CCK-8 assays) and (b) CLSM images (stained with FDA/PI for live/dead cells) of L929 cells cultured with 200 $\mu\text{g/mL}$ HA-control, HA/ALG-0.2%, and HA/ALG-0.4% NPs for 1, 3, and 5 days, respectively.

electric conductivity showed a slow and steady decline before 1.1 mL of NaOH added. It means that the existence of ALG would consume more OH^- to react with Ca^{2+} to form CaP completely. In addition, with a higher ALG addition, the curve slope of the initial decrease period gradually reduced to a lower value, specifying that more ions remained in the relevant reaction solutions. Correspondingly, the minimal value of conductivity elevated with a higher addition of ALG, further confirming the inhibition role of ALG in CaP formation.

On the basis of these results, we proved that ALG would inhibit the formation of CaP and proposed the possible regulation process of ALG on the growth of HA nanocrystals in this system. At the first stage, the ALG solution was mixed with CaCl_2 solution. Because ALG could easily cross-link with Ca^{2+} ions forming the “egg-box” structure, this process would provide nucleated sites for facilitating the crystal growth. After that, Na_2HPO_4 solution and NaOH solution were added for HA crystal formation. During this progress, Ca^{2+} ions cross-linked with ALG were attached to PO_4^{3-} and OH^- by electrostatic interaction first. Because of the presence of ALG, the formation of CaP compound was partly inhibited. After being stirred by physical crushing, the Ca-ALG gel was mixed enough with PO_4^{3-} and become a homogeneous blend. With the continuous reaction, the ALG would react with the CaP compound sufficiently, gel networks were capable of supporting the growing crystals, preventing sedimentation⁴² and controlling the rate of the process of Ca/P transform into HA. Because of this inhibition role of ALG, smaller and self-assembled HA NPs with lower crystallinity are obtained in the presence of a higher ALG concentration.

3.3. Cell Cytotoxicity of HA NPs. For biomedical applications, the cytotoxicity is of utmost importance. Figure 9 shows the cytotoxicity of synthesized HA/ALG NPs against L929 fibroblast cells. The biosafety of HA and ALG has been proved in many reports. Here, L929 cells were incubated with 200 $\mu\text{g/mL}$ HA-control, HA/ALG-0.2%, and HA/ALG-0.4% NPs for 1, 3, and 5 days, respectively. The CCK-8 results (Figure 9a) illustrate that all the NPs are biocompatible materials. Meanwhile, HA NPs synthesized with a higher ALG concentration gave the higher cell proliferation result. The growth of cells cultured with HA/ALG NPs was also visually observed with a confocal laser scanning microscope. CLSM images (Figure 9b) show that the cells incubated with different NPs all present a normal spreading morphology after culturing for 1, 3, and 5 days. Compared to HA-control, a higher number of live cells are observed when cultured with HA/ALG NPs,

further confirming the improved cytocompatibility of HA with ALG incorporation.

4. CONCLUSIONS

In summary, we have demonstrated a simple method to prepare stable, biocompatible, crystallinity-controlled, and size-controlled needle-like HA/ALG NPs. The addition of ALG makes the HA NPs more stable and dispersive in water. XRD, FT-IR, TGA, zeta potential, TEM/HRTEM, and BET results allow us to study the properties of synthesized HA nanohybrids and to propose a mechanism for the growth of HA nanocrystals. We have confirmed the regulation role of ALG to the HA NPs in RT and obtained a smaller size HA/ALG NPs with a higher specific surface area and negative charge, which make these needle-like HA NPs potentially applicable to delivery systems. In addition, we have discussed the regulation performance of ALG to the formation of calcium phosphate by monitoring the changes of pH value, conductivity, and Ca^{2+} concentration. Moreover, the HA/ALG NPs have an excellent biocompatibility when cultured with L929 cells, which ensure the biosafety of these HA/ALG NPs in further biomedical research.

AUTHOR INFORMATION

Corresponding Authors

*E-mail: guobohx@163.com (B.G.).

*E-mail: xli20004@yahoo.com. Phone: +86 (0) 28 85412102 (X.L.).

ORCID

Zeng Yi: 0000-0003-0473-2746

Xudong Li: 0000-0002-7939-5150

Notes

The authors declare no competing financial interest.

ACKNOWLEDGMENTS

This work is supported by the National Key Research and Development Program of China (no. 2016YFC1102700), the Sichuan Science and Technology Program Key Projects (no. 2017JY0018), and the National Basic Research Program of China (no. 2012CB933600).

REFERENCES

- (1) Li, C.; Born, A.-K.; Schweizer, T.; Zenobi-Wong, M.; Cerruti, M.; Mezzenga, R. Amyloid-hydroxyapatite bone biomimetic composites. *Adv. Mater.* **2014**, *26*, 3207–3212.
- (2) Puvvada, N.; Panigrahi, P. K.; Pathak, A. Room temperature synthesis of highly hemocompatible hydroxyapatite, study of their

physical properties and spectroscopic correlation of particle size. *Nanoscale* **2010**, *2*, 2631–2638.

(3) Li, B.; Kan, L.; Zhang, X.; Li, J.; Li, R.; Gui, Q.; Qiu, D.; He, F.; Ma, N.; Wang, Y.; Wei, H. Biomimetic Bone-like Hydroxyapatite by Mineralization on Supramolecular Porous Fiber Networks. *Langmuir* **2017**, *33*, 8493–8502.

(4) Sun, X.; Su, W.; Ma, X.; Zhang, H.; Sun, Z.; Li, X. Comparison of the osteogenic capability of rat bone mesenchymal stem cells on collagen, collagen/hydroxyapatite, hydroxyapatite and biphasic calcium phosphate. *Regener. Biomater.* **2018**, *5*, 93–103.

(5) Lin, K.; Xia, L.; Gan, J.; Zhang, Z.; Chen, H.; Jiang, X.; Chang, J. Tailoring the nanostructured surfaces of hydroxyapatite bioceramics to promote protein adsorption, osteoblast growth, and osteogenic differentiation. *ACS Appl. Mater. Interfaces* **2013**, *5*, 8008–8017.

(6) Ferraz, M. P.; Monteiro, F. J.; Manuel, C. M. Hydroxyapatite nanoparticles: a review of preparation methodologies. *J. Appl. Biomater. Biomech.* **2004**, *2*, 74–80.

(7) Palazzo, B.; Iafisco, M.; Laforgia, M.; Margiotta, N.; Natile, G.; Bianchi, C. L.; Walsh, D.; Mann, S.; Roveri, N. Biomimetic hydroxyapatite–drug nanocrystals as potential bone substitutes with antitumor drug delivery properties. *Adv. Funct. Mater.* **2007**, *17*, 2180–2188.

(8) Motkin, M.; Wright, D. M.; Muller, K.; Kyle, N.; Gard, T. G.; Porter, A. E.; Skepper, J. N. Hydroxyapatite nano and microparticles: correlation of particle properties with cytotoxicity and biostability. *Biomaterials* **2009**, *30*, 3307–3317.

(9) Ghosh, S. K.; Datta, S.; Roy, S. K. Solution Combustion Synthesis of Calcium Hydroxyapatite Nanoparticles. *Trans. Indian Ceram. Soc.* **2014**, *63*, 27–32.

(10) Bastakoti, B.; Hsu, Y.-C.; Liao, S.-H.; Wu, K. C.-W.; Inoue, M.; Yusa, S.-i.; Nakashima, K.; Yamauchi, Y. Inorganic–Organic Hybrid Nanoparticles with Biocompatible Calcium Phosphate Thin Shells for Fluorescence Enhancement. *Chem.—Asian J.* **2013**, *8*, 1301–1305.

(11) Sun, C.-Y.; Ma, Y.-C.; Cao, Z.-Y.; Li, D.-D.; Fan, F.; Wang, J.-X.; Tao, W.; Yang, X.-Z. Effect of Hydrophobicity of Core on the Anticancer Efficiency of Micelles as Drug Delivery Carriers. *ACS Appl. Mater. Interfaces* **2014**, *6*, 22709–22718.

(12) Yang, Y.-H.; Liu, C.-H.; Liang, Y.-H.; Lin, F.-H.; Wu, K. C.-W. Hollow mesoporous hydroxyapatite nanoparticles (hmHANPs) with enhanced drug loading and pH-responsive release properties for intracellular drug delivery. *J. Mater. Chem. B* **2013**, *1*, 2447–2450.

(13) Bastakoti, B. P.; Inoue, M.; Yusa, S.-i.; Liao, S.-H.; Wu, K. C.-W.; Nakashima, K.; Yamauchi, Y. A block copolymer micelle template for synthesis of hollow calcium phosphate nanospheres with excellent biocompatibility. *Chem. Commun.* **2012**, *48*, 6532–6534.

(14) Shi, Z.; Huang, X.; Cai, Y.; Tang, R.; Yang, D. Size effect of hydroxyapatite nanoparticles on proliferation and apoptosis of osteoblast-like cells. *Acta Biomater.* **2009**, *5*, 338–345.

(15) Cai, Y.; Liu, Y.; Yan, W.; Hu, Q.; Tao, J.; Zhang, M.; Shi, Z.; Tang, R. Role of hydroxyapatite nanoparticle size in bone cell proliferation. *J. Mater. Chem.* **2007**, *17*, 3780–3787.

(16) Zhao, H.; Li, X.; Wang, J.; Qu, S.; Weng, J.; Zhang, X. Characterization of Peroxide Ions in Hydroxyapatite Lattice. *J. Biomed. Mater. Res.* **2000**, *52*, 157.

(17) Chen, Z.; Zhou, H.; Wang, X.; Sang, L.; Wang, C.; Ma, J.; Li, X. Controlled mineralization by extracellular matrix: monodisperse, colloidal stable calcium phosphate-hyaluronan hybrid nanospheres. *Chem. Commun.* **2010**, *46*, 1278–1280.

(18) An, L.; Li, W.; Xu, Y.; Zeng, D.; Cheng, Y.; Wang, G. Controlled additive-free hydrothermal synthesis and characterization of uniform hydroxyapatite nanobelts. *Ceram. Int.* **2016**, *42*, 3104–3112.

(19) Fang, W.; Zhang, H.; Yin, J.; Yang, B.; Zhang, Y.; Li, J.; Yao, F. Hydroxyapatite Crystal Formation in the Presence of Polysaccharide. *Cryst. Growth Des.* **2016**, *16*, 1247–1255.

(20) Wang, X. M.; Wang, X. L.; Ma, J. F.; Jiang, J. M.; Zheng, G. Q.; Chen, Z. H.; Li, X. D. Versatile Nanostructured Processing Strategy for Bone Grafting Nanocomposites Based on Collagen Fibrillogenesis. *Adv. Appl. Ceram.* **2009**, *108*, 384–388.

(21) Ma, X.; Peng, W.; Su, W.; Yi, Z.; Chen, G.; Chen, X.; Guo, B.; Li, X. Delicate Assembly of Ultrathin Hydroxyapatite Nanobelts with Nanoneedles Directed by Dissolved Cellulose. *Inorg. Chem.* **2018**, *57*, 4516–4523.

(22) Katz, E.; Willner, I. Integrated nanoparticle–biomolecule hybrid systems: synthesis, properties, and applications. *Angew. Chem., Int. Ed.* **2004**, *43*, 6042–6108.

(23) Parak, W. J.; Gerion, D.; Pellegrino, T.; Zanchet, D.; Micheel, C.; Williams, S. C.; Boudreau, R.; Le Gros, M. A.; Larabell, C. A.; Alivisatos, A. P. Biological applications of colloidal nanocrystals. *Nanotechnology* **2003**, *14*, R15.

(24) Luo, D.; Sang, L.; Wang, X.; Xu, S.; Li, X. Low Temperature, pH-Triggered Synthesis of Collagen–Chitosan–Hydroxyapatite Nanocomposites as Potential Bone Grafting Substitutes. *Mater. Lett.* **2011**, *65*, 2395–2397.

(25) Gombotz, W. R.; Wee, S. F. Protein release from alginate matrices. *Adv. Drug Delivery Rev.* **2012**, *64*, 194–205.

(26) Sang, L.; Luo, D.; Xu, S.; Wang, X.; Li, X. Fabrication and evaluation of biomimetic scaffolds by using collagen–alginate fibrillar gels for potential tissue engineering applications. *Mater. Sci. Eng., C* **2011**, *31*, 262–271.

(27) van den Berg, F.; Lyndgaard, C. B.; Sørensen, K. M.; Engelsen, S. B. Process analytical technology in the food industry. *Trends Food Sci. Technol.* **2013**, *31*, 27–35.

(28) Sang, L.; Huang, J.; Luo, D.; Chen, Z.; Li, X. Bone-like nanocomposites based on self-assembled protein-based matrices with Ca²⁺ capturing capability. *J. Mater. Sci.: Mater. Med.* **2010**, *21*, 2561–2568.

(29) Sun, Z.; Yi, Z.; Zhang, H.; Ma, X.; Su, W.; Sun, X.; Li, X. Bio-responsive alginate-keratin composite nanogels with enhanced drug loading efficiency for cancer therapy. *Carbohydr. Polym.* **2017**, *175*, 159–169.

(30) Tonnesen, H. H.; Karlsen, J. Alginate in drug delivery systems. *Drug Dev. Ind. Pharm.* **2002**, *28*, 621–630.

(31) Chen, J.; Chen, Z.; Wang, C.; Li, X. Calcium-assisted hydrothermal carbonization of an alginate for the production of carbon microspheres with unique surface nanopores. *Mater. Lett.* **2012**, *67*, 365–368.

(32) Wang, L.; Li, Y.; Li, C. In situ processing and properties of nanostructured hydroxyapatite/alginate composite. *J. Nanopart. Res.* **2008**, *11*, 691–699.

(33) Teng, S.; Shi, J.; Peng, B.; Chen, L. The effect of alginate addition on the structure and morphology of hydroxyapatite/gelatin nanocomposites. *Compos. Sci. Technol.* **2006**, *66*, 1532–1538.

(34) Draget, K. I.; Skjåk-Bræk, G.; Smidsrød, O. Alginate based new materials. *Int. J. Biol. Macromol.* **1997**, *21*, 47–55.

(35) Matthew, I. R.; Browne, R. M.; Frame, J. W.; Millar, B. G. Subperiosteal behaviour of alginate and cellulose wound dressing materials. *Biomaterials* **1995**, *16*, 275–278.

(36) Mierisch, C. M.; Cohen, S. B.; Jordan, L. C.; Robertson, P. G.; Balian, G.; Diduch, D. R. Transforming growth factor- β in calcium alginate beads for the treatment of articular cartilage defects in the rabbit. *Arthroscopy* **2002**, *18*, 892–900.

(37) Parhi, P.; Ramanan, A.; Ray, A. R. Preparation and characterization of alginate and hydroxyapatite-based biocomposite. *J. Appl. Polym. Sci.* **2006**, *102*, 5162–5165.

(38) Kithva, P. H.; Grøndahl, L.; Kumar, R.; Martin, D.; Trau, M. An organic matrix-mediated processing methodology to fabricate hydroxyapatite based nanostructured biocomposites. *Nanoscale* **2009**, *1*, 229–232.

(39) Son, K. D.; Yang, D. J.; Kim, M. S.; Kang, I.-K.; Kim, S. Y.; Kim, Y.-J. Effect of alginate as polymer matrix on the characteristics of hydroxyapatite nanoparticles. *Mater. Chem. Phys.* **2012**, *132*, 1041–1047.

(40) Eiselt, P.; Yeh, J.; Latvala, R. K.; Shea, L. D.; Mooney, D. J. Porous carriers for biomedical applications based on alginate hydrogels. *Biomaterials* **2000**, *21*, 1921–1927.

(41) Liang, Y.-H.; Liu, C.-H.; Liao, S.-H.; Lin, Y.-Y.; Tang, H.-W.; Liu, S.-Y.; Lai, I.-R.; Wu, K. C.-W. Diffusion characteristics of calcium

alginate gels. Cosynthesis of Cargo-Loaded Hydroxyapatite/Alginate Core–Shell Nanoparticles (HAP@Alg) as pH-Responsive Nano-vehicles by a Pre-gel Method. *ACS Appl. Mater. Interfaces* **2012**, *4*, 6720–6727.

(42) Wang, L.; Li, Y.; Li, C. In situ processing and properties of nanostructured hydroxyapatite/alginate composite. *J. Nanopart. Res.* **2009**, *11*, 691–699.

(43) Lin, H.-R.; Yeh, Y.-J. Porous alginate/hydroxyapatite composite scaffolds for bone tissue engineering: preparation, characterization, and in vitro studies. *J. Biomed. Mater. Res., Part B* **2004**, *71*, 52–65.

(44) Coleman, R. J.; Jack, K. S.; Perrier, S.; Grøndahl, L. Hydroxyapatite mineralization in the presence of anionic polymers. *Cryst. Growth Des.* **2013**, *13*, 4252–4259.

(45) Wang, Y.; Ren, X.; Ma, X.; Su, W.; Zhang, Y.; Sun, X.; Li, X. Alginate-intervened hydrothermal synthesis of hydroxyapatite nanocrystals with nanopores. *Cryst. Growth Des.* **2015**, *15*, 1949–1956.

(46) Morris, E. R.; Rees, D. A.; Thom, D.; Boyd, J. Chiroptical and stoichiometric evidence of a specific, primary dimerisation process in alginate gelation. *Carbohydr. Res.* **1978**, *66*, 145–154.

(47) Ming, J.; Jiang, Z.; Wang, P.; Bie, S.; Zuo, B. Silk fibroin/sodium alginate fibrous hydrogels regulated hydroxyapatite crystal growth. *Mater. Sci. Eng., C* **2015**, *51*, 287–293.